Lawrence Berkeley National Laboratory
Recent Work

Title
Unravelling surface and interfacial structures of a metal-organic framework by transmission electron microscopy.

Permalink

Journal

ISSN

Authors
Zhu, Yihan
Ciston, Jim
Zheng, Bin
et al.

Publication Date

DOI

Peer reviewed

Unravelling surface and interfacial structures of a metal–organic framework by transmission electron microscopy

Yihan Zhu[1]*, Jim Ciston[2], Bin Zheng[3], Xiaohe Miao[4], Cory Czarnik[5], Yichang Pan[1], Rachid Sougrat[4], Zhiping Lai[1], Chia-En Hsiung[1], Kexin Yao[1], Ingo Pinnau[1], Ming Pan[5]* and Yu Han[1]*

Metal–organic frameworks (MOFs) are crystalline porous materials with designable topology, porosity and functionality, having promising applications in gas storage and separation, ion conduction and catalysis[1-3]. It is challenging to observe MOFs with transmission electron microscopy (TEM) due to the extreme instability of MOFs upon electron beam irradiation[4-7]. Here, we use a direct-detection electron-counting camera to acquire TEM images of the MOF ZIF-8 with an ultralow dose of 4.1 electrons per square ångström to retain the structural integrity. The obtained image involves structural information transferred up to 2.1 Å, allowing the resolution of individual atomic columns of Zn and organic linkers in the framework. Furthermore, TEM reveals important local structural features of ZIF-8 crystals that cannot be identified by diffraction techniques, including armchair-type surface terminations and coherent interfaces between assembled crystals. These observations allow us to understand how ZIF-8 crystals self-assemble and the subsequent influence of interfacial cavities on mass transport of guest molecules.

The periodic, crystallographic structures of MOFs are mainly solved by diffraction-based techniques[8-11]. However, like other crystalline materials, MOF crystals inevitably contain local, non-periodic structural features, such as surfaces, interfaces, defects and disorder, which are, from an application perspective, equally important as the crystallographic structure and can dominate the overall properties of mass transport, sorption and catalysis[12-14]. There is a need to develop a technique to probe the local structures of MOFs with sufficiently high resolution[15].

High-resolution TEM (HRTEM) is a powerful tool for observing local structures[16-18]; however, HRTEM is conventionally unsuitable for MOFs because electron beams immediately destroy their structures. To date, several studies have reported TEM imaging of some typical MOF materials, including MIL-101 (ref. 4), MOF-5 (ref. 6), UiO-66 (ref. 5) and ZIF-8 (ref. 7). However, only primary channels were resolved by the limited resolution, as a result of instantaneous degradation of the structure during imaging[4-6]. Cryo-TEM was used in a case study of MOF-5 to minimize beam damage caused by the heating effect[6], but it failed to provide marked improvement in resolution. In a recent study of Zn-MOF-74 (ref. 19), Cs-corrected scanning TEM (STEM) discriminated ordered Zn clusters in the framework but individual Zn atomic columns and organic linkers remained unresolved, implying that MOFs are also vulnerable under STEM conditions. In principle, MOFs can be imaged with HRTEM by using sufficiently low electron doses to retain their structures; however, in practice conventional scintillator-based charge-coupled device cameras cannot produce enough signal-to-noise ratio under sufficiently low-dose conditions to render useful images[20].

Here, we demonstrate that the recent invention of direct-detection electron-counting cameras provides an effective solution to this problem. The high detective quantum efficiency[20] of these cameras allows HRTEM to be performed with an extremely low electron beam dose, making it possible to directly image beam-sensitive materials with minimal structural degradation. This advantage has led to multiple breakthroughs in structural biology[21]. In this work, by combining regular TEM with a direct-detection electron-counting camera (Gatan K2 Summit) we were able to acquire an HRTEM image of the MOF material ZIF-8 with ultralow electron dose to capture its intact structure before damage occurred. We achieve information transfer up to 2.1 Å, which allows for observing local structures with high precision to provide new insights into the self-assembly mechanism of ZIF-8 and its defect-mediated mass transport properties.

ZIF-8 has a framework formula of $Zn(2\text{-methylimidazole})_2$ and a sodalite topology with a space group of $I\bar{4}3m$, containing large cages (11.6 Å in diameter) connected through 6-ring windows (3.4 Å) (Fig. 1a,b)[3]. The ZIF-8 crystals examined in this work are uniform in size (∼85 ± 15 nm) and shape. These crystals are highly vulnerable to electron beam illumination: their crystallinity is quickly lost when the accumulated electron dose reaches $\sim 25\,e^-\,Å^{-2}$, as evidenced by the fading of electron diffraction spots (Supplementary Fig. 1). To prevent structural damage during sample searching, we reviewed the specimen in the diffraction mode to render enough contrast at a dose rate as low as $\sim 1\,e^-\,Å^{-2}\,s^{-1}$. Even under such low-dose conditions, the structure of ZIF-8 crystals quickly began to degrade; therefore, immediate image acquisition upon initial inspection was required. We successively took TEM images at a high frame rate (40 fps) and then merged the 120 frames exposed in 3 seconds with accurate correction of sample motion to restore the high-resolution structural information (Supplementary Fig. 2).

[1]King Abdullah University of Science and Technology (KAUST), Advanced Membranes and Porous Materials Center, Physical Sciences and Engineering Division, Thuwal 23955-6900, Saudi Arabia. [2]National Center for Electron Microscopy, Molecular Foundry, Lawrence Berkeley National Laboratory, Berkeley, California 94720, USA. [3]School of Materials Science and Engineering, Xi'an University of Science and Technology, Xi'an 710054, China. [4]King Abdullah University of Science and Technology (KAUST), Imaging and Characterization Core Lab, Thuwal 23955-6900, Saudi Arabia. [5]Gatan, Inc., Pleasanton, California 94588, USA. *e-mail: yihan.zhu@kaust.edu.sa; mpan@gatan.com; yu.han@kaust.edu.sa

1

A motion-corrected image taken along the [111] axis of a ZIF-8 crystal is shown in the upper inset of Fig. 1c and Supplementary Fig. 3, of which the total electron dose was 4.1 e⁻ Å⁻² and the pixel size was 0.86 Å. We determined the defocus value of the image to be −550 nm by analysing the Fresnel fringe that appeared at the crystal's edge (Supplementary Fig. 4). According to the TEM simulation using this defocus value, the hexagonally arranged white dots in the image (Fig. 1c) represent the 6-ring channels of ZIF-8 (Supplementary Fig. 5). Fast Fourier transform (FFT) of this image indicates information transfer as high as 2.1 Å (Fig. 1c, bottom inset), far exceeding the HRTEM resolutions reported for MOFs in previous studies. By monitoring the reflection intensity in FFT, we confirmed that the structural information at both low and high spatial frequencies remained intact in successive frames used for integrating the image (Supplementary Fig. 6). The appearance of 2.1 Å reflection in the FFT is a testament to the structural integrity of ZIF-8 under the low-dose conditions used. We processed the image using the determined defocus value to correct the 'contrast inversion' associated with the contrast transfer function (CTF) of the objective lens. While this method does not fully treat multiple scattering, the extremely low density of MOFs greatly decreases their effective scattering thickness. From the more interpretable CTF-corrected image[22], individual Zn atomic columns in triplet that are ~3.4 Å apart from each other and imidazole rings with two different configurations (edge-on/face-on) in the ZIF-8 structure were identified after denoising either by Wiener filtering (Fig. 1d) or by real-space averaging (Supplementary Fig. 7). Despite a slight distortion observed for Zn triplets in the raw image, imposing a projection symmetry ($p31m$) to the lattice-averaged image results in a very good match to the projected structural model and potential map of ZIF-8 along the [111] direction (Fig. 1d and Supplementary Fig. 8). This result demonstrates the feasibility of atomic-resolution TEM of an intact MOF structure under carefully chosen imaging conditions and thus provides a basis for the following analysis of the crystal surface and interface. It should be noted that the image processing methods we used have been meticulously analysed and validated (see Supplementary Figs 9 and 10).

Scanning electron microscopy (Supplementary Fig. 11) revealed that ZIF-8 crystals have a rhombic dodecahedral shape. Hence, (110) surfaces are the exposed surfaces whose termination can be directly imaged along the [111] incidence (that is, an edge-on configuration)[18]. As viewed from this direction, the (110) surface of ZIF-8 may form a 'zigzag' or 'armchair'-type termination with the surface Zn^{2+} ions capped by 2-methylimidazole (Hmim) (Supplementary Fig. 12). Our HRTEM results show that the (110) surfaces of ZIF-8 crystals terminate smoothly without reconstruction or macro-defects (Fig. 2a). By comparing the experimental image with the simulated HRTEM images for the two types of surface termination in terms of the shape, thickness and position of Fresnel fringes (Supplementary Fig. 13), we conclude that the surface is terminated in the armchair model (Fig. 2b,c). Although the armchair-type termination produces more dangling ligands, our calculations reveal that it leads to a lower surface energy than does the zigzag termination (2.04 versus 2.43 J m⁻²), probably because of the formation of Hmim hydrogen bonding (N–H···N) chains (Supplementary Fig. 12). Strong contrast from Fresnel fringes and aberration-induced image delocalization inhibits a more detailed structural analysis of the topmost Zn layer.

ZIF-8 crystals were reported to self-assemble through oriented attachment driven by van der Waals attractions[23] or dipole–dipole interactions[24]. Interestingly, rhombic dodecahedral ZIF-8 crystals were 'locked' at (110) interfaces after attachment, while this phenomenon was not observed for cubic ZIF-8 crystals that interact via (100) surfaces[24], indicating that (110) surfaces are particularly important for self-assembly. Our HRTEM image allowed us to investigate the (110) interfacial structure between two ZIF-8 crystals
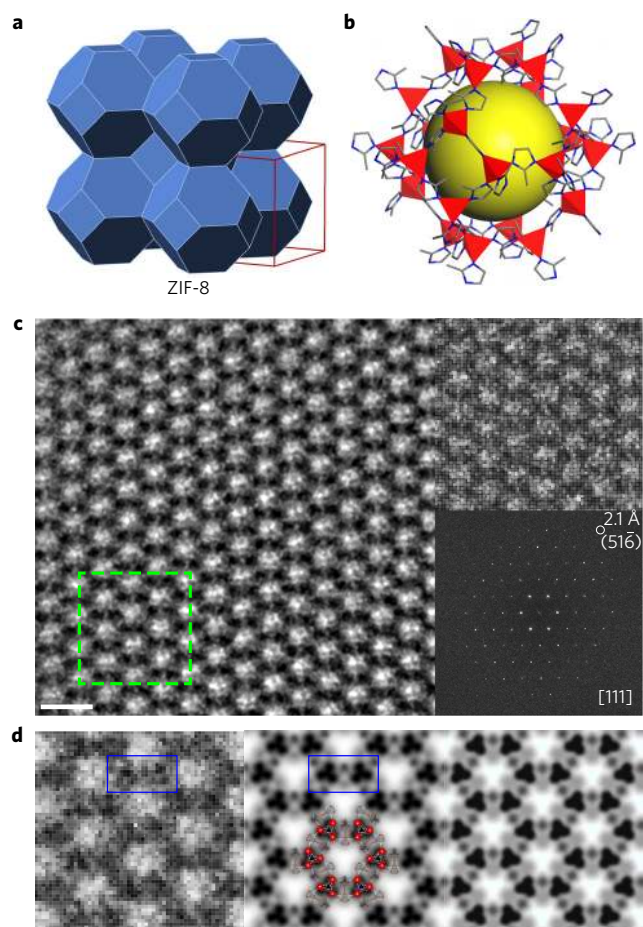

Figure 1 | Atomic-resolution imaging of the ZIF-8 crystal lattice.
a, Topological model of ZIF-8. **b**, A ZIF-8 sodalite cage: yellow represents void space, red is the ZnN_4 tetrahedra, and grey and blue represent C and N atoms, respectively. H atoms are omitted for clarity. **c**, HRTEM image of ZIF-8 along the [111] axis (scale bar, 2 nm). This image is cropped from the original drift-corrected image shown in Supplementary Fig. 3, rotated and denoised using a Wiener filter. The upper and lower insets are the unfiltered image with a pixel size of 0.86 Å and the FFT, respectively. **d**, Left, CTF-corrected and denoised (using a Wiener filter) image of the region within the green square in **c**; middle, symmetry-imposed and lattice-averaged image with a structural model of ZIF-8 embedded; right, simulated projected potential map with a point spread function width of 2.1 Å, where dark contrast refers to high potential values. Blue rectangles highlight representative regions where individual atomic columns of Zn and imidazole rings can be identified.

at an unprecedented resolution (Fig. 3). A low-magnification TEM image shows the oriented attachment of two ZIF-8 crystals via (110) surfaces (Fig. 3b), where a seamless transitional interface is clearly observed. The (1̄12) lattice fringes of the two crystals are perfectly aligned with each other (Fig. 3a) across the interface, as if a single crystal splits into two parts that are slightly pulled away from the interface without tilting or rotating. The HRTEM image denoised by real-space averaging clearly shows that the two interconnecting (110) surfaces are both of the armchair type (Supplementary Fig. 14), reaffirming our conclusion about surface termination. The image also reveals that the two surfaces are attached in an arm-to-notch configuration, which further confirms that the interface structure highly coheres with the bulk structure of ZIF-8 except for the presence of a slight separation that breaks the continuity of the lattice throughout the two crystals. The degree of the separation (along the normal of the interface) between the two
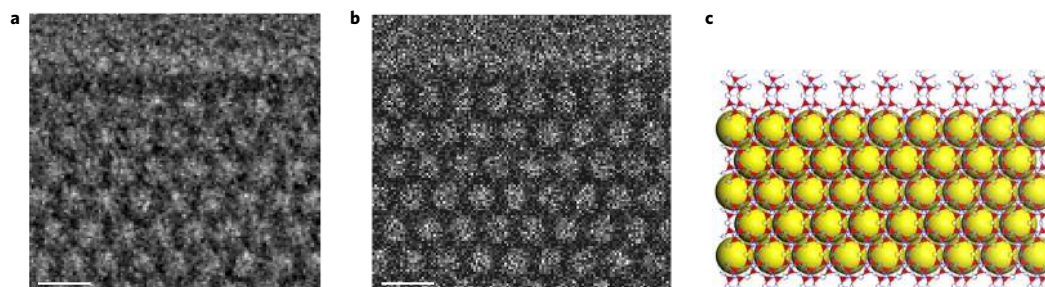
Figure 2 | Surface termination of ZIF-8 crystals. a,b, Experimental (**a**) and simulated (**b**) HRTEM images of ZIF-8 taken along the [111] axis containing the (110) surface (scale bar, 2 nm). **c,** Optimized structural model of the ZIF-8 (110) surface by density-functional-based tight-binding methods.
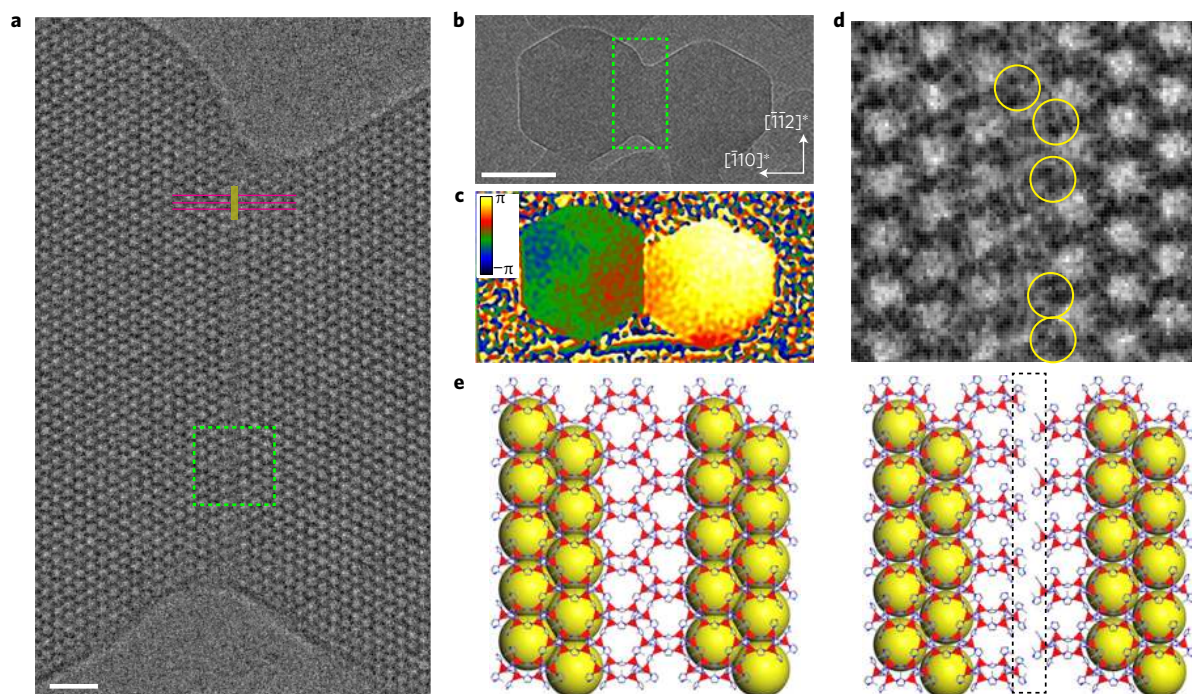

Figure 3 | Coherent interface formed between two assembled ZIF-8 crystals. a, HRTEM image of the green rectangular interface region in **b** along the [111] axis (scale bar, 5 nm). Purple lines are used to show the coherence between the ($\bar{1}\bar{1}2$) lattice fringes in the two crystals that are separated by an interface represented by the yellow line. **b,** Low-magnification TEM image of two oriented, attached ZIF-8 crystals (scale bar, 50 nm). **c,** The corresponding geometric phase map of the $\mathbf{g}_{1\bar{1}0}$ reciprocal lattice vector rendered in temperature colour codes. **d,** CTF-corrected HRTEM image of the region within the green square in **a**. Yellow circles highlight Zn triplets with obvious distortions. **e,** Bulk (left) and optimized interfacial structures (right) projected along the [111] direction showing the identical arrangement of the lattice except for the existence of an additional layer of ligands (and subsequent hydrogen bonds) in the interface, as marked by the black dashed rectangle.

crystals relative to a perfect single crystal can be more accurately determined by geometric phase analysis of the $\mathbf{g}_{1\bar{1}0}$ reciprocal lattice vector that is perpendicular to the interface. The geometric phase map clearly shows a phase shift of the right crystal with respect to the left one by $2\pi/3 \sim \pi$, corresponding to a separation distance of $0.4 \sim 0.6$ nm (Fig. 3c). We observed the same coherent interface on another pair of attached ZIF-8 crystals (Supplementary Fig. 15), suggesting that this interfacial structure is a universal feature of the oriented attachment between ZIF-8 crystals via (110) surfaces.

The coherent interface indicates that the assembly of ZIF-8 crystals is unlikely driven solely by non-directional van der Waals forces[25]. Meanwhile, the interfacial displacement we observed corresponds to an additional layer of ligands at the interface with respect to the perfect crystal structure, suggesting direct adhesion of two ligand-terminated surfaces without chemical reactions (Fig. 3e). Hence, we attempted to reproduce the self-assembly process of two armchair-terminated ZIF-8 crystal slabs by molecular dynamics simulations (Supplementary Fig. 16). The results show that the

formation of an arm-to-notch interfacial structure is mediated by an arm-to-arm (twinning-like) configuration as a local energy minimum. Two crystals are attracted by long-range van der Waals forces that seek to maximize the contact between crystals. Directional hydrogen bonding occurs at the post-contact stage to form multiple N–H···N bonds between two layers of terminal ligands. The two crystals are thus irreversibly locked. This process results in a coherent interface (Supplementary Fig. 17), which agrees well with our HRTEM observations. The atomic interface structure, as optimized by density-functional-based tight-binding methods, exhibits a displacement of 0.6 nm along the [110] direction relative to a continuous lattice, also consistent with that determined from HRTEM (Supplementary Fig. 17). Accordingly, the simulated HRTEM image of the optimized interface structure matches well with the experimental image (Supplementary Fig. 14). Note that according to the simulated interface structure, there is a displacement (0.6 nm) between the two crystals along the [111] direction, which is required for the formation of hydrogen bonds but cannot be observed in
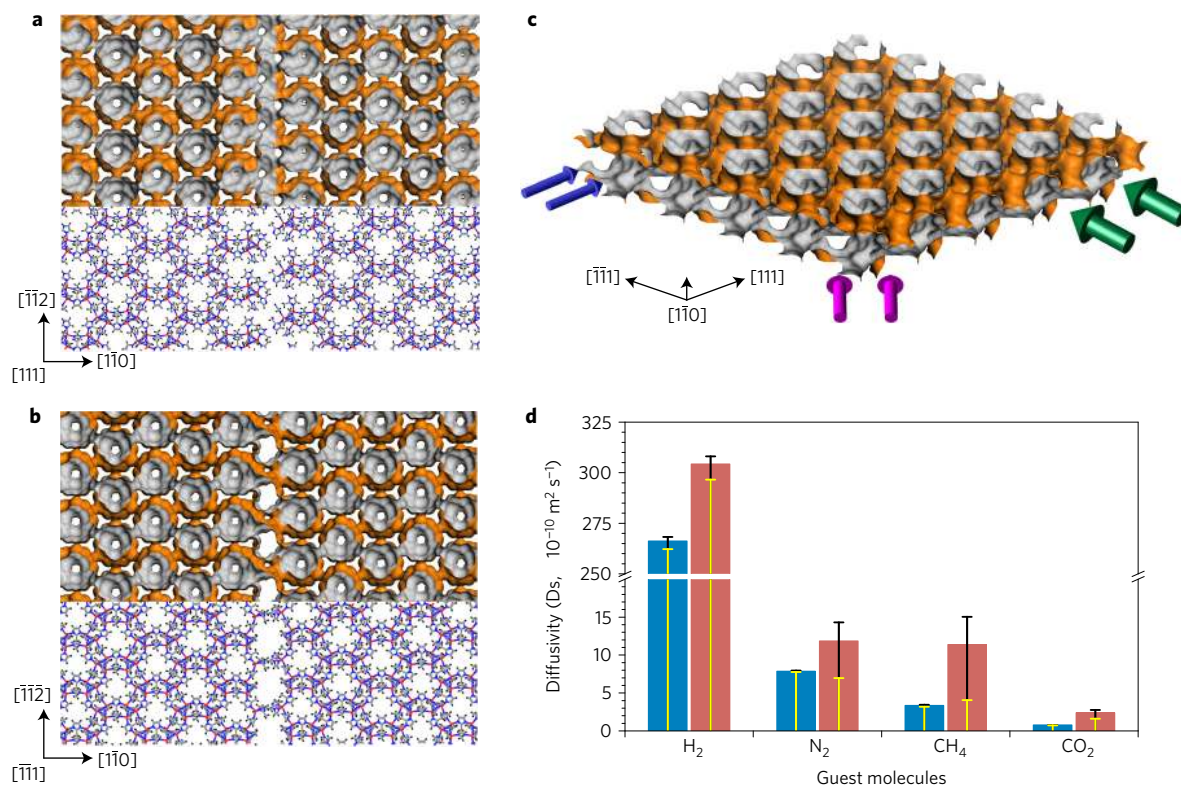
Figure 4 | Formation of interfacial cavities between assembled ZIF-8 crystals and their influences on gas diffusion. a,b, Structural projections showing the interface between assembled ZIF-8 crystals along the [111] (**a**) and [$\bar{1}\bar{1}$1] (**b**) directions. Each projection is represented by Connolly surfaces with a probe radius of 1.82 Å (upper) and a ball-and-stick model (lower). Zn, C, N and H atoms are labelled in red, blue, grey, and black, respectively. **c,** Visualization of interfacial cavities by a Connolly surface. One-dimensional channels with different widths along [$\bar{1}\bar{1}$1] (8.2 Å), [001] (3.8 Å) and [111] (2.6 Å) directions are marked by green, purple and blue arrows, respectively. **d,** Calculated self-diffusivities (D_s) of different guest molecules at a loading of six molecules per unit cell in the bulk (blue) and interface-containing (red) flexible ZIF-8 frameworks at 300 K by molecular dynamics simulations. Anisotropic diffusivities within and perpendicular to the interface plane are labelled as black and yellow bars.

the [111] projected TEM image. Furthermore, individual atomic columns of Zn can be identified in a CTF-corrected image of a local interfacial region, where they exhibit distortions compared with their crystallographic geometries, as highlighted by the yellow circles in the image (Fig. 3d). According to our simulations, this can be associated with various surface point defects, such as dangling linkers and linker vacancies (Supplementary Fig. 18).

Self-assembly of ZIF-8 crystals is a common phenomenon that plays an important role in the fabrication of various gas-separation membranes. The interfacial structure illustrated by HRTEM provides a basis for modelling how the assembly of ZIF-8 crystals affects their mass transport properties. The interconnection of two ZIF-8 crystals via (110) surfaces opens up sodalite cages on both sides of the interface and creates larger cavities. Figure 4 presents the optimized interfacial structure with Connolly surfaces and wireframe models in different projections. In the bulk regions, the sodalite cages are straightly aligned along the [111] axis (Fig. 4a) and the symmetry-equivalent [$\bar{1}\bar{1}$1] axis (Fig. 4b). However, the interface layer has different projections in these two directions due to its lower symmetry. The largest pore openings along the [111] direction have a diameter of only ~2.6 Å (Fig. 4a). In contrast, one-dimensional channels (~8.2 Å in diameter) that are significantly wider than the inherent 6-ring pores of ZIF-8 (3.4 Å) are formed at the interface along the [$\bar{1}\bar{1}$1] direction (Fig. 4b). As illustrated in Fig. 4c, there also exists a set of channels (~3.8 Å) in the interface layer along the [001] direction. The two groups of channels both extend within the interface layer and are interconnected with each other. There are no straight channels across the interface, that is, along the [1$\bar{1}$0] direction (Fig. 4c). We calculated self-diffusivities for H_2, N_2, CO_2

and CH_4 guest molecules within both bulk and interface-containing flexible ZIF-8 frameworks by molecular dynamics simulations, and the results are summarized in Fig. 4d and Supplementary Table 1. The inclusion of interfacial cavities remarkably increased the diffusivities of all guest molecules at different loadings, owing to the large interfacial channel openings. For instance, the diffusivity of CH_4 increases from 3.35×10^{-10} to 11.38×10^{-10} m^2 s^{-1} at a loading of six molecules per unit cell. Larger guest molecules exhibit a greater increase in diffusivity. The self-diffusion of guest molecules has a remarkable anisotropy in the interface-containing framework, because of the much faster diffusion within the interface layer than across it. To experimentally verify the role of interfacial pores in mass transport, we measured the kinetic vapour adsorption of toluene and 1,3,5-trimethylbenzene (TMB) to calculate their transport diffusivities (D_t) over four ZIF-8 samples that were prepared to have different degrees of interfacial porosity by controlling the crystal size, shape and assembly (Supplementary Figs 19–22). Despite their distinct morphologies, the two samples without interfacial porosity exhibited almost the same diffusivity in the cases of both toluene and TMB adsorption, indicating that intrinsic pore structure dominated mass transport in these two samples. By comparison, the sample with maximal interfacial porosity showed twofold and fourfold higher D_t values for toluene and TMB respectively, and the sample with fewer interfacial pores showed medium diffusivity (Supplementary Table 2). These results corroborate the conclusion of our simulation that the interfacial pore structure can alleviate the diffusion limitations of ZIF-8 against bulky molecules.

In summary, with the assistance of HRTEM, we provide insights into the self-assembly mechanism, surface termination modes, and

interfacial structures of a representative MOF material ZIF-8. These characteristics are directly connected to the diffusivity of gases in ZIF-8, implying a defect-driven structure–property relationship between interfaces and mass transport. We also demonstrate that the combination of TEM and a direct-detection electron-counting camera is a powerful tool for observing not only the bulk crystalline structures but also the local, non-periodic structures of electron-beam-sensitive materials. This study paves the way for HRTEM imaging on materials such as zeolites, MOFs, covalent organic frameworks, polymers and two-dimensional materials.

Methods

Methods, including statements of data availability and any associated accession codes and references, are available in the online version of this paper.

References

1. Li, H., Eddaoudi, M., O'Keeffe, M. & Yaghi, O. M. Design and synthesis of an exceptionally stable and highly porous metal–organic framework. *Nature* **402**, 276–279 (1999).
2. Furukawa, H., Cordova, K. E., O'Keeffe, M. & Yaghi, O. M. The chemistry and applications of metal–organic frameworks. *Science* **341**, 974–986 (2013).
3. Park, K. S. *et al*. Exceptional chemical and thermal stability of zeolitic imidazolate frameworks. *Proc. Natl Acad. Sci. USA* **103**, 10186–10191 (2006).
4. Lebedev, O. I., Millange, F., Serre, C., Van Tendeloo, G. & Ferey, G. First direct imaging of giant pores of the metal–organic framework MIL-101. *Chem. Mater.* **17**, 6525–6527 (2005).
5. Zhu, L. K., Zhang, D. L., Xue, M., Li, H. & Qiu, S. L. Direct observations of the MOF (UiO-66) structure by transmission electron microscopy. *Crystengcomm* **15**, 9356–9359 (2013).
6. Wiktor, C., Turner, S., Zacher, D., Fischer, R. A. & Van Tendeloo, G. Imaging of intact MOF-5 nanocrystals by advanced TEM at liquid nitrogen temperature. *Micropor. Mesopor. Mat.* **162**, 131–135 (2012).
7. Cravillon, J. *et al*. Rapid room-temperature synthesis and characterization of nanocrystals of a prototypical zeolitic imidazolate framework. *Chem. Mater.* **21**, 1410–1412 (2009).
8. Feyand, M. *et al*. Automated diffraction tomography for the structure elucidation of twinned, sub-micrometer crystals of a highly porous, catalytically active bismuth metal–organic framework. *Angew. Chem. Int. Ed.* **51**, 10373–10376 (2012).
9. Yakovenko, A. A., Reibenspies, J. H., Bhuvanesh, N. & Zhou, H. C. Generation and applications of structure envelopes for porous metal–organic frameworks. *J. Appl. Crystallogr.* **46**, 346–353 (2013).
10. Adams, C. J., Haddow, M. F., Lusi, M. & Orpen, A. G. Crystal engineering of lattice metrics of perhalometallate salts and MOFs. *Proc. Natl Acad. Sci. USA* **107**, 16033–16038 (2010).
11. Wu, H. *et al*. Unusual and highly tunable missing-linker defects in zirconium metal–organic framework UiO-66 and their important effects on gas adsorption. *J. Am. Chem. Soc.* **135**, 10525–10532 (2013).
12. Fang, Z. L., Bueken, B., De Vos, D. E. & Fischer, R. A. Defect-engineered metal–organic frameworks. *Angew. Chem. Int. Ed.* **54**, 7234–7254 (2015).
13. Makiura, R. *et al*. Surface nano-architecture of a metal–organic framework. *Nat. Mater.* **9**, 565–571 (2010).
14. Song, Q. L. *et al*. Zeolitic imidazolate framework (ZIF-8) based polymer nanocomposite membranes for gas separation. *Energy Environ. Sci.* **5**, 8359–8369 (2012).
15. Cliffe, M. J. *et al*. Correlated defect nanoregions in a metal–organic framework. *Nat. Commun.* **5**, 4176–4183 (2014).
16. Zhu, Y. H. *et al*. Atomic resolution imaging of nanoscale structural ordering in a complex metal oxide catalyst. *Chem. Mater.* **24**, 3269–3278 (2012).
17. Hashimoto, A., Suenaga, K., Gloter, A., Urita, K. & Iijima, S. Direct evidence for atomic defects in graphene layers. *Nature* **430**, 870–873 (2004).
18. Zhu, Y. H., Wang, Q. X., Zhao, L. & Han, Y. Direct observation of surface reconstruction and termination on a complex metal oxide catalyst by electron microscopy. *Angew. Chem. Int. Ed.* **51**, 4176–4180 (2012).
19. Mayoral, A., Sanchez-Sanchez, M., Alfayate, A., Perez-Pariente, J. & Diaz, I. Atomic observations of microporous materials highly unstable under the electron beam: the cases of Ti-doped AlPO$_4$-5 and Zn-MOF-74. *Chemcatchem* **7**, 3719–3724 (2015).
20. Li, X. M. *et al*. Electron counting and beam-induced motion correction enable near-atomic-resolution single-particle cryo-EM. *Nat. Methods* **10**, 584–590 (2013).
21. Bartesaghi, A. *et al*. 2.2 angstrom resolution cryo-EM structure of beta-galactosidase in complex with a cell-permeant inhibitor. *Science* **348**, 1147–1151 (2015).
22. Zou, X. D., Hovmöller, S. & Oleynikov, P. *Electron Crystallography: Electron Microscopy and Electron Diffraction* (Oxford Univ. Press, 2011).
23. Yanai, N. & Granick, S. Directional self-assembly of a colloidal metal–organic framework. *Angew. Chem. Int. Ed.* **51**, 5638–5641 (2012).
24. Yanai, N., Sindoro, M., Yan, J. & Granick, S. Electric field-induced assembly of monodisperse polyhedral metal–organic framework crystals. *J. Am. Chem. Soc.* **135**, 34–37 (2013).
25. Utama, M. I. B. *et al*. Recent developments and future directions in the growth of nanostructures by van der Waals epitaxy. *Nanoscale* **5**, 3570–3588 (2013).

Author contributions

Y.Z. and Y.H. conceived and designed the experiments. J.C. and M.P. performed the low-dose high-resolution TEM image acquisition. Y.Z., J.C., M.P. and Y.H. carried out the TEM image processing, analysis and simulation. Y.Z., B.Z. and X.M. performed the theoretical simulations. Y.P., Z.L. and R.S. prepared the samples for imaging. C.-E.H. synthesized the ZIF-8 samples of various sizes and shapes. K.Y. and I.P. performed kinetic vapour adsorption experiments. Y.Z. drafted the manuscript and Y.H., J.C., M.P. and C.C. revised it. All authors commented on the manuscript.

Additional information

Supplementary information is available in the online version of the paper. Reprints and permissions information is available online at www.nature.com/reprints. Correspondence and requests for materials should be addressed to Y.Z., M.P. or Y.H.

Competing financial interests

The authors declare no competing financial interests.

Methods

The synthetic methods of various ZIF-8 samples are provided in the Supplementary Methods.

Low-dose TEM image acquisition. TEM images were taken on an uncorrected FEI Titan 80–300 electron microscope with a Cs of 1.2 mm, a convergence angle of 0.2 mrad and a focal spread of 4.5 nm at 300 kV. The specimen searching was carried out in diffraction mode with a dose rate as low as ∼1 e$^-$ Å^{-2} s^{-1} and then quickly switched to image mode for immediate image acquisition.

Low-dose TEM images were acquired by a Gatan K2 direct-detection camera operated in electron-counting mode (camera counting frame rate of 400 fps (frames per second) at 4 k × 4 k resolution) with a final image output rate of 40 fps at 4 k × 4 k resolution. An exposure of 3 s therefore results in an image stack of 120 individual image frames. These frames can be summed to improve the signal-to-noise ratio (SNR) and correct for sample motion during the exposure. At the microscope nominal magnification of ×43 k, the pixel size of the acquired images was calibrated as 0.86 Å.

TEM image processing and simulation. *CTF-correction of HRTEM images.* The contrast of the raw HRTEM image cannot be directly interpreted as the chemical structure because of modulations by the CTF of the objective lens at a specific defocus. This effect can be compensated for by using a CTF filter function implemented in CRISP software[26]. This causes a shift in phase of all information between CTF crossovers by π in the complex FFT map. The CTF-corrected image can be then derived by inverse FT of the filtered FFT map. The defocus value was determined by the Fresnel fringe analysis as demonstrated in Supplementary Fig. 4.

Extraction of lattice-averaged and symmetry-imposed projected electrostatic potential. The HRTEM image over a bulk crystal structure region was first processed by refining the lattice on the basis of the (1$\bar{1}$0) and (0$\bar{1}$1) reflections as lattice vectors using CRISP software, followed by the extraction of structure factor amplitudes and phases from all reflections averaged over the whole region. The extracted amplitudes and phases were then symmetrized by the projection symmetry *p*31*m* of the crystal structure and used for the reconstruction of the projected potential map.

Real-spacing averaging of image motifs. To improve the SNR of the interface structures, an interfacial small region as the motif was chosen from the image shown in Fig. 3a (see Supplementary Fig. 14a). Cross-correlation of this motif with the original image was calculated along the interface. The cross-correlation function reveals the exact locations of the motif where it repeats itself. A special routine for finding the local intensity maxima was carried out in DigitalMicrograph software (http://www.gatan.com). Using the cross-correlation function, the motif was averaged along the interface (Supplementary Fig. 14b). The improvement in SNR for the averaged motif is proportional to the square root of the number of motifs averaged[27]. In our case, a total of 29 motifs were averaged; thus, the SNR was improved by about a factor of 5.

HRTEM image and projected potential map simulation. HRTEM simulation was performed by using the multislice method implemented in QSTEM software (http://www.qstem.org) that uses Dirac–Fock ionic scattering potentials[28]. The imaging condition and aberration coefficients were set according to the experimental parameters. Specifically, a 300 kV accelerating voltage, a convergence angle of 0.2 mrad, a Cs of 1.2 mm, and a focal spread of 4.5 nm were used. Specimen thickness was selected as 100 nm, similar to that observed for the as-synthesized ZIF-8 crystals. The pixel size of the simulated HRTEM image was adjusted to 0.86 Å according to the experimentally acquired image. Experimental image noise predominantly coming from the electron beam shot noise was simulated in MATLAB by introducing randomness to the image using a Poisson random variable based on each pixel value. The projected potential map of ZIF-8 structure along the [111] direction was also simulated using QSTEM software and a point spread function width of 2.1 Å.

Data availability. All data included in this study are available from the corresponding authors on request.

References

26. Hovmoller, S. CRISP: crystallographic image processing on a personal computer. *Ultramicroscopy* **41,** 121–135 (1992).
27. Pan, M. & Crozier, P. A. Low-dose high-resolution electron-microscopy of zeolite materials with a slow-scan CCD camera. *Ultramicroscopy* **48,** 332–340 (1993).
28. Rez, D., Rez, P. & Grant, I. Dirac–Fock calculations of X-ray scattering factors and contributions to the mean inner potential for electron-scattering. *Acta Crystallogr. A* **50,** 481–497 (1994).